INTERNATIONAL JOURNAL FOR NUMERICAL METHODS IN FLUIDS
Int. J. Numer. Meth. Fluids 2008; **57**:1603–1627
Published online 8 December 2007 in Wiley InterScience (www.interscience.wiley.com). DOI: 10.1002/fld.1688

High-order $\mathscr{C}^1$ finite-element interpolating schemes—Part I: Semi-Lagrangian linear advection

G. Djoumna*, †, R. Pierre and D. Y. Le Roux

Département de Mathématiques et de Statistique, Université Laval, Québec, Canada G1K 7P4

SUMMARY

This paper is devoted to the development of accurate high-order interpolating schemes for semi-Lagrangian advection. The characteristic-Galerkin formulation is obtained by using a semi-Lagrangian temporal discretization of the total derivative. The semi-Lagrangian method requires high-order interpolators for accuracy. A class of $\mathscr{C}^1$ finite-element interpolating schemes is developed and two semi-Lagrangian methods are considered by tracking the feet of the characteristic lines either from the interpolation or from the integration nodes. Numerical stability and analytical results quantifying the amount of artificial viscosity induced by the two methods are presented in the case of the one-dimensional linear advection equation, based on the modified equation approach. Results of test problems to simulate the linear advection of a cosine hill illustrate the performance of the proposed approach. Copyright © 2007 John Wiley & Sons, Ltd.

Received 25 May 2007; Revised 12 October 2007; Accepted 14 October 2007

KEY WORDS: advection equation; characteristic-Galerkin method; finite-element method; semi-Lagrangian method, modified equation

1. INTRODUCTION

The advection equation has been for many years an active area of research in the computational fluid dynamics community. This type of equation is not simple to solve numerically due to the fact that the transport process takes place along the characteristic lines and that the information comes from the past [1–4]. The transport equation has been solved employing mainly three families of numerical schemes: the Eulerian, the Lagrangian and the Eulerian–Lagrangian methods [5–11].

*Correspondence to: Georges Djoumna, Département de Mathématiques et de Statistique, Université Laval, Québec, QC, Canada G1K 7P4.
†E-mail: gdjoumna@mat.ulaval.ca

Contract/grant sponsor: Natural Sciences and Engineering Research Council (NSERC)
Contract/grant sponsor: Fonds québécois de la recherche sur la nature et les technologies (FQRNT)

A version of the Eulerian–Lagrangian scheme also known as the semi-Lagrangian method is used in the present study.

The semi-Lagrangian advection scheme combines the gridpoint nature of Eulerian schemes (regular resolution) with the enhanced stability of Lagrangian methods, and the treatment of time and space are intimately linked [12]. The semi-Lagrangian scheme usually offers the possibility of using time steps that exceed those permitted by the Courant–Friedrichs–Lewy (CFL) stability criterion for Eulerian discretizations of advection-dominated flows. The CFL condition ensures that the domain of dependence of the analytical solution of a hyperbolic partial differential equation (PDE) is contained within the domain of dependence of the numerical solution. For advection-dominated flows, a time discretization in a semi-Lagrangian framework can circumvent the CFL bound associated with Eulerian advection. The semi-Lagrangian advection scheme shifts the numerical domain of dependence, in the form of a finite-difference stencil, to the grid cell containing the upstream departure point of the fluid particle trajectory, thus permitting Courant numbers that can exceed unity. They can be considered to be equivalent to Eulerian methods that are shifted upwind by the advecting velocity. The possibility of stable integration with Courant numbers exceeding unity is not the only virtue of a semi-Lagrangian advection scheme. It also gives good phase speeds with little numerical dispersion when compared with Eulerian schemes.

The accuracy of a semi-Lagrangian advection scheme depends on the choice of an interpolation method. Two semi-Lagrangian schemes are presented in this study. In the first case, one uses the characteristic stemming backward from the interpolation nodes, called the *interpolation semi-Lagrangian finite-elements method* (ISLFEM), while in the second case, one uses those stemming from the quadrature nodes, named here *quadrature semi-Lagrangian finite-element method* (QSLFEM). The latter has already been used in [2, 8, 11].

The purpose of this paper is to develop an accurate cost-effective high-order interpolation scheme to solve advection problems. Various interpolator schemes have been used in the past in regular domains; these include linear, quadratic, cubic and quintic Lagrange polynomials, bicubic splines and compact and non-compact methods [1, 11]. The bicubic spline interpolation, which gives fourth-order spatial truncation errors with little damping, has been found to be a good compromise between accuracy and computational cost for short-term simulations in the context of atmospheric models [13–16]. In [17, 18] the kriging method has been used as a proof-of-concept test and was found to yield equally high-order accuracy results on regular grids and unstructured meshes. However, to our knowledge, there is a lack of interpolation error analysis for the kriging scheme in the literature.

In this paper, we take a first step toward the development of a class of accurate $\mathscr{C}^1$-interpolating methods, based on finite-element schemes that are used to solve fourth-order problems [19]. Such an approach is expected to lead to accurate and flexible interpolating schemes that could be easily implemented in two and three dimensions.

The paper is divided as follows. The characteristic-Galerkin method for the transport equation and the semi-Lagrangian schemes are described in Sections 2 and 3, respectively. In Section 4 a stability and accuracy analysis of the semi-Lagrangian methods is performed by using the modified equation approach of Warming and Hyett [20]. Two classes of $\mathscr{C}^1$-interpolating methods are then introduced in Section 5: the Hsieh–Clough–Tocher and Bell families. Results of linear advection experiments to simulate the propagation of a cosine hill employing the proposed two methods and their computational cost are discussed in Section 6. Conclusions are drawn in Section 7.

DOI: 10.1002/fld

2. THE CHARACTERISTIC-GALERKIN METHOD FOR LINEAR TRANSPORT EQUATION

Let Ω be a regular open-bounded domain of $\mathbb{R}^m$ with Lipschitz boundary $\partial\Omega$. Functional spaces are defined using standard Sobolev space notations. In particular, $H^1(\Omega)$ is the space of functions in the square integrable space $L^2(\Omega)$, whose first derivatives belong to $L^2(\Omega)$.

For a vector field $\mathbf{A}(\mathbf{x},t)$ defined on $\bar{\Omega}$ (the closure set of Ω), we name inward boundary the subsect $\Gamma^-_{\mathbf{A}(\mathbf{x},t)}$ of $\partial\Omega$ defined as

$$\Gamma^-_{\mathbf{A}(\mathbf{x},t)}=\{\mathbf{x}\in\partial\Omega\,|\,\mathbf{A}(\mathbf{x},t)\cdot\mathbf{n}<0\}$$

where $\mathbf{x}$ is the position vector, t is the time variable and $\mathbf{n}$ is the unit outward normal with respect to $\partial\Omega$.

In the following the divergence and gradient operators are defined with respect to the space variables only. The vector field $\mathbf{A}$ is assumed to be divergence free and to belong to $L^\infty(\Omega\times[0,T])$. Let T be a nonzero positive real number. Given g defined on $\partial\Omega$ and f, U_0 defined on Ω, we consider the following advection problem: find $U(\mathbf{x},t)$ in $H^1(\Omega)$ such that

$$\frac{\partial U}{\partial t}(\mathbf{x},t)+\mathbf{A}(\mathbf{x},t)\cdot\nabla U(\mathbf{x},t)=f(\mathbf{x},t)\quad\text{in }\Omega\times]0,T[\tag{1}$$

$$U(\mathbf{x},0)=U_0\quad\text{in }\Omega \tag{2}$$

$$U(\mathbf{x},t)=g(\mathbf{x},t)\quad\forall\mathbf{x}\in\Gamma^-_{\mathbf{A}(\mathbf{x},t)}\ \ \forall t\in]0,T[\tag{3}$$

The Lagrangian coordinate $\mathbf{X}=\mathbf{X}(\mathbf{x},t;\tau)$ provides the position at time τ of a particule that has been driven by the field $\mathbf{A}(\mathbf{x},t)$ and that occupied the position $\mathbf{x}$ at the time t. It is the solution of the Cauchy problem:

$$\frac{\mathrm{d}\mathbf{X}}{\mathrm{d}\tau}(\mathbf{x},t;\tau)=\mathbf{A}(\mathbf{X}(\mathbf{x},t;\tau),\tau) \tag{4}$$

$$\mathbf{X}(\mathbf{x},t;t)=\mathbf{x} \tag{5}$$

with $0<\tau<t$. When $\mathbf{A}$ is a velocity field, $\mathbf{X}$ is the characteristic path or trajectory.

By using (4) and (5), Equation (1) is rewritten as

$$\frac{\mathrm{D}U}{\mathrm{D}t}(\mathbf{x},t)=\frac{\partial U}{\partial\tau}(\mathbf{X}(\mathbf{x},t;\tau),\tau)|_{\tau=t}=f(\mathbf{X}(\mathbf{x},t;\tau),\tau)|_{\tau=t}=f(\mathbf{x},t) \tag{6}$$

For a given time step $\Delta t=t_{n+1}-t_n$, $n=0,1,\ldots,N$, where N is a positive integer, $t_n=n\Delta t$ and $t_N=T=N\Delta t$, the left-hand side (LHS) of (6) is discretized by employing the backward Euler scheme and this leads to

$$\frac{1}{\Delta t}(U(\mathbf{x},t_{n+1})-U(\mathbf{X}(\mathbf{x},t_{n+1};t_n),t_n))\approx\left(\frac{\partial U}{\partial t}+\mathbf{A}\cdot\nabla U\right)_{(\mathbf{x},t_{n+1})} \tag{7}$$

by taking into account that $\mathbf{X}(\mathbf{x},t_{n+1};t_{n+1})=\mathbf{x}$.

Let us denote an approximation of $\mathbf{X}(\mathbf{x},t_{n+1};t_n)$ by $\mathbf{X}^n$. One can typically choose the forward Euler scheme to discretize (4) and obtain

$$\mathbf{X}^n(\mathbf{x})=\mathbf{x}-\Delta t\mathbf{A}^n(\mathbf{x}) \tag{8}$$

when $\mathbf{A}^n(\mathbf{x})=\mathbf{A}(\mathbf{x},t_n)$. With this choice, $\mathbf{X}^n$ is a second-order approximation of $\mathbf{X}(\mathbf{x},t_{n+1};t_n)$.

DOI: 10.1002/fld

Equation (1) is then discretized using the characteristic method and this leads to

$$\frac{1}{\Delta t}(U^{n+1}(\mathbf{x})-U^n(\mathbf{X}^n))=f(\mathbf{x},t_{n+1}) \quad \text{in } \Omega \tag{9}$$

where U^n is the numerical approximation in time of $U(\mathbf{x},t_n)$. In order to discretize (9) in space, we denote the subspace of functions in $H^1(\Omega)$, by $H^1_{\Gamma_0}(\Omega)$, which vanish on a subset Γ_0 of $\partial\Omega$ of positive measure. Let $\mathscr{L}_h$ be a triangulation of Ω and let P_{k,Γ_0} be the finite-element subspace

$$P_{k,\Gamma_0}=\{p\in\mathscr{C}^0(\bar{\Omega})\,|\,p|_{\Gamma_0}=0,\ p|_K\in P_k(K),\forall K\in\mathscr{L}_h\}$$

where $P_k(K)$ denotes the space of polynomials of degree k on K.

The weak formulation of (9) requires that we search for U_h belonging to P_{k,Γ_0} such that

$$\int_\Omega U_h^{n+1}(\mathbf{x})\phi_h\,\mathrm{d}\mathbf{x}=\int_\Omega U_h^n(\mathbf{X}^n)\phi_h\,\mathrm{d}\mathbf{x}+\Delta t\int_\Omega f(\mathbf{x},t_{n+1})\phi_h\,\mathrm{d}\mathbf{x}\quad\forall\phi_h\in P_{k,\Gamma_0} \tag{10}$$

where the test function ϕ_h also belongs to P_{k,Γ_0}, and $\mathrm{d}\mathbf{x}$ is the area element.

Scheme (10) is convergent in the L^2-norm for $k=1$ with the resulting error $O(h^2+h^2\Delta t^{-1}+\Delta t)$, as shown in [4, 9].

3. THE SEMI-LAGRANGIAN ADVECTION SCHEME

While most Eulerian methods treat time and space as though they were unrelated, with exceptions such as the Lax–Wendroff scheme, characteristic methods interpret the time derivative at mesh nodal locations as the rate of change along flow characteristics. Similarly, the semi-Lagrangian advection is treated using time differences along particle trajectories. The essence of this hybrid treatment is to simultaneously combine the advantages of regular meshes of Eulerian schemes with the enhanced stability of Lagrangian methods. It usually permits the use of a longer time step than that allowed by the CFL stability criterion. The semi-Lagrangian scheme for advection (see [6, 7, 12, 21], e.g. in the context of environmental studies) is a generalization of (10) as shown in [22], and we introduce the method by rewriting (1) in the form

$$\frac{\mathrm{D}U}{\mathrm{D}t}\equiv\frac{\partial U}{\partial t}+\mathbf{A}\cdot\nabla U=f(\mathbf{x},t) \tag{11}$$

A different set of particles is selected at each time step, and we require that at the end of the time step, they arrive precisely at the mesh nodes. By tracking the particle back over that time step, we can locate its position at the previous time step using an approximate trajectory. An interpolation procedure is then used to determine the upstream value of an advected scalar field. A review of semi-Lagrangian integration schemes can be found in [7].

A schematic for the two-time-level semi-Lagrangian scheme [21], that has $O(\Delta t^2)$ accuracy, is shown in Figure 1 in one dimension. The straight line $(A'C)$ approximates the exact trajectory (AC), both of which arrive at mesh point x_m at time $t_n+\Delta t$. The particle is displaced by the

DOI: 10.1002/fld

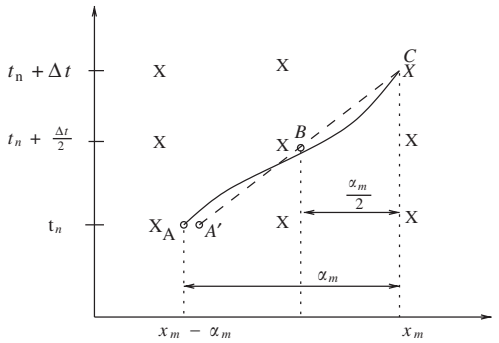

Figure 1. A two-time-level semi-Lagrangian advection scheme. Approximate (A′C) and exact (AC) trajectories arrive at node x_m at time $t_n+\Delta t$. Here, $\boldsymbol{\alpha}_m$ is the displacement of the particle in the x-direction at time Δt.

distance $\boldsymbol{\alpha}_m$ during the time step Δt. The total time derivative at mesh nodes is simply the rate of change along flow characteristics. A semi-Lagrangian approximation to (11) and (4) is

$$\frac{1}{\Delta t}(U^{n+1}(\mathbf{x}_m)-U^n(\mathbf{x}_m-\boldsymbol{\alpha}_m))=f \tag{12}$$

Equation (12) is nothing else than (9) where $\mathbf{X}^n$ is obtained from (8) with $\boldsymbol{\alpha}_m=\mathbf{X}(t_{n+1})-\mathbf{X}(t_n)$, and $\mathbf{A}$ is now the velocity field. Thus, $U^n(\mathbf{X}^n)$ in (9) is rewritten as $U^n(\mathbf{x}_m-\boldsymbol{\alpha}_m)$ in (12). The right-hand side (RHS) in (12) can be evaluated at point $(\mathbf{x}_m, t_{n+1})$ as in (9) but also at point $(\mathbf{x}_m-\boldsymbol{\alpha}_m/2, t_n+\Delta t/2)$, for example.

The weak formulation of (12) is then obtained from (10)

$$\int_\Omega U_h^{n+1}(\mathbf{x}_m)\phi_h\,\mathrm{d}\mathbf{x}=\int_\Omega U_h^n(\mathbf{x}_m-\boldsymbol{\alpha}_m)\phi_h\,\mathrm{d}\mathbf{x}+\Delta t\int_\Omega f\phi_h\,\mathrm{d}\mathbf{x}\quad\forall\phi_h\in P_{k,\Gamma_0} \tag{13}$$

The displacements $\boldsymbol{\alpha}_m$ are determined by an approximate integration of the characteristic curves defined in (4). Once $\boldsymbol{\alpha}_m$ is calculated, the solution is obtained by evaluating U_h^n at $\mathbf{x}_m-\boldsymbol{\alpha}_m$. The calculation of $\boldsymbol{\alpha}_m$ and $U_h^n(\mathbf{x}_m-\boldsymbol{\alpha}_m)$ is mainly obtained by using the two following approaches: the ISLFEM and the QSLFEM methods that are now described.

3.1. The ISLFEM

The first approach is called the ISLFEM and it is used in [4, 8, 15–17, 21]. By tracking back a particle located at an *interpolation node* (e.g. node C in Figure 1) over a time step, we can locate its position at the previous time step using an approximate trajectory (e.g. (A′C) in Figure 1). In order to compute the displacement $\boldsymbol{\alpha}_m$ at each interpolation node, we need to solve (4)

$$\boldsymbol{\alpha}_m\equiv\mathbf{X}(t_{n+1})-\mathbf{X}(t_n)=\int_{t_n}^{t_{n+1}}\mathbf{A}(\mathbf{X}(s),s)\,\mathrm{d}s \tag{14}$$

Using the second-order Runge–Kutta method, we obtain the following fixed point problem:

$$\boldsymbol{\alpha}_m=\Delta t\mathbf{A}\left(\mathbf{x}_m-\frac{\boldsymbol{\alpha}_m}{2},t_n+\frac{\Delta t}{2}\right) \tag{15}$$

DOI: 10.1002/fld

The first-order approximation $\boldsymbol{\alpha}_m = \Delta t \mathbf{A}^n(\mathbf{x})$ in (8) is rarely used in practice due to the inherent dissipation of first-order temporal schemes. In the following, we adopt the two-step algorithm introduced in [14, 21] to have sufficiently accurate $O(\Delta t^2)$ estimates of the trajectory:

(i) Extrapolate the velocity field at all interpolation nodes in (15) at time $(t_n + \Delta t/2)$ by using a two-time-level scheme

$$\tilde{\mathbf{A}}\left(\mathbf{x}_m, t_n + \frac{\Delta t}{2}\right) = \frac{3}{2}\mathbf{A}(\mathbf{x}_m, t_n) - \frac{1}{2}\mathbf{A}(\mathbf{x}_m, t_n - \Delta t) + O(\Delta t^2) \tag{16}$$

(ii) For each interpolation node, a first-order estimate $\boldsymbol{\alpha}_m^0 = \Delta t \mathbf{A}(\mathbf{x}_m, t_n)$ is combined with a number of iterations of

$$\boldsymbol{\alpha}_m^{k+1} = \Delta t \tilde{\mathbf{A}}\left(\mathbf{x}_m - \frac{\boldsymbol{\alpha}_m^k}{2}, t_n + \frac{\Delta t}{2}\right), \quad k = 1, 2, 3, \ldots \tag{17}$$

using interpolation when evaluating the RHS. A sufficient condition for convergence of (17) is given in [23].

Finally, the ISLFEM procedure is completed by evaluating the first integral in the RHS of (13) following the five-step process:

(i) Obtain $U^n(\mathbf{x}_m)$ at each node $\mathbf{x}_m$ at time t_n.
(ii) Compute the displacement $\boldsymbol{\alpha}_m$ at each interpolation node at time t_n by using (17).
(iii) Interpolate $U^n(\mathbf{x}_m)$ at the upstream positions $(\mathbf{x}_m - \boldsymbol{\alpha}_m)$ using an interpolation scheme to obtain $\hat{U}^n$.
(iv) Expand $\hat{U}^n$ in terms of the basis functions as $\hat{U}^n = \sum_j \hat{U}_j^n \phi_j$ on each triangle K of $\mathscr{L}_h$.
(v) Compute the first integral in the RHS of (13) on K using a numerical quadrature

$$\int_K U_h^n(\mathbf{x}_m - \boldsymbol{\alpha}_m)\phi_i \, \mathrm{d}\mathbf{x} = \int_K \sum_j \hat{U}_j^n \phi_j \phi_i \, \mathrm{d}\mathbf{x} = \sum_j \sum_q \hat{U}_j^n \omega_q \phi_j(\xi_q)\phi_i(\xi_q) \tag{18}$$

where ω_q and ξ_q are the weights and nodes of the quadrature formula while i refers to the node equation.

The ISLFEM method is conditionally stable and may suffer from numerical dissipation. In this regard the interpolation step (iii) is crucial for the accuracy of the semi-Lagrangian scheme. The stability analysis is performed in Section 4.

3.2. The QSLFEM

The second method consists in evaluating the first term in the RHS of (13) at the foot of the characteristic lines by tracking back a particle located at an *integration node*. All the integrals in (13) are computed by numerical integration. Such an approach is named QSLFEM and it is conceptually different from the one used in Section 3.1. Indeed, rather than tracking back the particules from the interpolation nodes, the QSLFEM tracks the particules backwards from the quadrature (integration) nodes.

Since the particules are tracked backwards from the integration nodes, one needs to compute the displacement $\boldsymbol{\alpha}_m$ at each *integration node* and not at the interpolation nodes as in Section 3.1. Hence, $\boldsymbol{\alpha}_m$ is obtained as in (16) and (17) but $\mathbf{x}_m$ is now an integration node.

DOI: 10.1002/fld

The QSLFEM procedure is completed by evaluating the first integral in the RHS of (13) following the four-step process:

(i) Obtain $U^n(\mathbf{x}_m)$ at each node at time t_n, as for step (i) of Section 3.1.
(ii) Compute the displacement $\boldsymbol{\alpha}_m$ at each integration node at time t_n by using (17).
(iii) Calculate U_h^n at the upstream positions $\xi_q - \boldsymbol{\alpha}_m(\xi_q)$ using an interpolation scheme. As in Section 3.1 the present step is crucial for the accuracy of the method.
(iv) Compute the first integral in the RHS of (13) on triangle K using a numerical quadrature

$$\int_K U_h^n(\mathbf{x}_m - \boldsymbol{\alpha}_m(\mathbf{x}_m))\phi_i \, \mathrm{d}x = \sum_q \omega_q U_h^n(\xi_q - \boldsymbol{\alpha}_m(\xi_q))\phi_i(\xi_q) \tag{19}$$

The QSLFEM is generally less diffusive than the ISLFEM as first pointed out in [2] and later in [11]. More quantitative comparisons are given in Section 6. A very attractive property of the QSLFEM is its straightforward implementation in multiple dimensions. The QSLFEM may however lead to instabilities [11] and this problem is now considered.

4. STABILITY ANALYSIS OF ISLFEM *VERSUS* QSLFEM METHODS

In this section, a stability analysis of the ISLFEM and QSLFEM methods based on the modified PDE method introduced in [20] is presented. By using the amplification factor, Warming and Hyett [20] have shown the connection between the so-called 'heuristic' stability theory and the Von Newmann method. The essence of the modified equation approach is that, by examining a truncated version of that equation, various properties of a finite-difference scheme such as the order of accuracy and consistency can be deduced quite simply. Moreover, this method permits one to gain an insight into the nature of both dissipative and dispersive errors. The technique involves determining the actual PDE, which is solved numerically, aside from round-off errors by a given initial-value problem solver (see [20]).

The modified equation is derived by using a two-steps procedure described as follows: firstly, each term of a given finite-difference scheme is expanded using the Taylor series. A PDE is obtained, which includes an infinite number of spatial and time derivatives. Secondly, high-order time derivatives are eliminated by using algebraic operations [20].

For a given finite-difference scheme analogue of the PDE

$$\frac{\partial U}{\partial t} + \mathscr{J}_x(U) = 0 \tag{20}$$

where $\mathscr{J}_x(U)$ represents a linear spatial differential operator; the procedure described above provides the following equation:

$$\frac{\partial U}{\partial t} + \mathscr{J}_x(U) = \sum_p \mu(p) \frac{\partial^p U}{\partial x^p} \tag{21}$$

where the coefficient $\mu(p)$ stands for the coefficient of the pth spatial derivative.

For the remaining part of this section the modified equation approach is used to analyse the stability, diffusion, dispersion properties and the order of accuracy of the ISLFEM and QSLFEM

DOI: 10.1002/fld

approaches. We limit our study to linear finite-element approximation of (1) in the context of a one-dimensional advection problem with constant coefficients.

We assume that $\Omega=]0,1[$ and we assume that $f=0$ and $g=0$. The mesh is uniform and we let h be the mesh length parameter. The semi-Lagrangian discretization of (1) leads to

$$\frac{h}{6}(U_{i-1}^{n+1}+4U_i^{n+1}+U_{i+1}^{n+1})=\int_\Omega U_h^n(x-\alpha_m(x))\phi_i\,\mathrm{d}x \tag{22}$$

where U_h^n is a linear approximation to U^n and the LHS of (22) comes from to the mass matrix using linear finite elements. For the sake of simplicity, we assumed that the transport velocity A is a positive constant, the displacement field $\alpha_m=A\Delta t$ and the Courant number $c=A\Delta t/h$ is smaller than one. For a uniform space–time grid, we denote $s_j=jh$.

4.1. Interpolation methods

A stability analysis of IFESLM applied to (22) is performed in the following subsection. If the RHS of (22) is computed using a linear approximation at the foot of the characteristics, we obtain

$$\begin{aligned}\int_\Omega U^n(x-\alpha_m(x))\phi_i\,\mathrm{d}x &= U^n(s_{i-1}-A\Delta t)\int_0^1\phi_{i-1}\phi_i\,\mathrm{d}x\\ &\quad+U^n(s_i-A\Delta t)\int_0^1\phi_i^2\,\mathrm{d}x+U^n(s_{i+1}-A\Delta t)\int_0^1\phi_{i+1}\phi_i\,\mathrm{d}x\\ &=\frac{h}{6}(U^n(s_{i-1}-A\Delta t)+4U^n(s_i-A\Delta t)+U^n(s_{i+1}-A\Delta t))\end{aligned} \tag{23}$$

Employing a linear approximation for U^n leads to $U^n(s_i-A\Delta t)=(1-c)U_i^n+cU_{i-1}^n$, since $c<1$, and combining (22) and (23) we obtain

$$U_{i-1}^{n+1}+4U_i^{n+1}+U_{i+1}^{n+1}=(1-c)(U_{i-1}^n+4U_i^n+U_{i+1}^n)+c(U_{i-2}^n+4U_{i-1}^n+U_i^n) \tag{24}$$

The application of the modified equation approach to (24) is now presented. Let ϕ satisfy

$$\frac{\partial\phi}{\partial t}+A\frac{\partial\phi}{\partial x}=0 \tag{25}$$

then the truncation error $\varepsilon_h(\phi)$ associated with (24) is expressed as

$$\begin{aligned}\Delta t\,\varepsilon_h(\phi)&=\phi(s_{i-1},t^{n+1})+4\phi(s_i,t^{n+1})+\phi(s_{i+1},t^{n+1})\\ &\quad-(1-c)(\phi(s_{i-1},t^n)+4\phi(s_i,t^n)+\phi(s_{i+1},t^n))\\ &\quad-c(\phi(s_{i-2},t^n)+4\phi(s_{i-1},t^n)+\phi(s_i,t^n))\end{aligned} \tag{26}$$

DOI: 10.1002/fld

Owing to a Taylor expansion of $\varepsilon_h(\phi)$ at the vicinity of the point (s_i, t^n), we have

$$\Delta t\,\varepsilon_h(\phi) = 6\Delta t\frac{\partial\phi}{\partial t} + 6c\frac{\partial\phi}{\partial x} + 3\Delta t^2\frac{\partial^2\phi}{\partial t^2} + h^2\Delta t\frac{\partial^3\phi}{\partial x^2\partial t} + \Delta t^3\frac{\partial^3\phi}{\partial t^3} + \frac{1}{2}h^2\Delta t^2\frac{\partial^4\phi}{\partial x^2\partial t^2}$$
$$+\frac{1}{4}\Delta t^4\frac{\partial^4\phi}{\partial t^4} - 3ch^2\frac{\partial^2\phi}{\partial x^2} - \frac{3}{4}ch^4\frac{\partial^4\phi}{\partial x^4} + 2ch^3\frac{\partial^3\phi}{\partial x^3} + O(h^5) + O(\Delta t^5) \tag{27}$$

Higher-order derivatives in time can be expressed in terms of spatial derivatives of the same order by using (25)

$$\frac{\partial^m\phi}{\partial t^m} = (-1)^m A^m\frac{\partial^m\phi}{\partial x^m} \tag{28}$$

where m is a positive integer. This leads to

$$\varepsilon_h(\phi) = 3(-1+c)h\frac{\partial^2\phi}{\partial x^2} + (1-c^2)h^2\frac{\partial^3\phi}{\partial x^3} + O(h^3) \tag{29}$$

The scheme is thus of order one in space. The modified equation then reads

$$\frac{\partial\phi}{\partial t} + A\frac{\partial\phi}{\partial x} + hD(\phi) = 0 \tag{30}$$

where the operator D is defined below.

By using (28), Equation (27) is rewritten as

$$\Delta t\,\varepsilon_h(\phi) = 6\Delta t\left(\frac{\partial\phi}{\partial t} + A\frac{\partial\phi}{\partial x}\right) + 3\Delta t^2\frac{\partial^2\phi}{\partial t^2} - 3ch^2\frac{\partial^2\phi}{\partial x^2} + \Delta t^3\frac{\partial^3\phi}{\partial t^3} + h^2\Delta t\frac{\partial^3\phi}{\partial x^2\partial t}$$
$$+\frac{1}{2}h^2\Delta t^2\frac{\partial^4\phi}{\partial x^2\partial t^2} + \frac{1}{4}\Delta t^4\frac{\partial^4\phi}{\partial t^4} - \frac{3}{4}ch^4\frac{\partial^4\phi}{\partial x^4} + 2ch^3\frac{\partial^3\phi}{\partial x^3} + O(h^5) + O(\Delta t^5) \tag{31}$$

Thanks to (30), we finally obtain

$$\varepsilon_h(\phi) = -6hD(\phi) + 3A(c-1)\frac{\partial^2\phi}{\partial x^2}h + O(h^2) \tag{32}$$

If $\varepsilon_h(\phi) = O(h^2)$ then

$$D(\phi) = \frac{1}{2}(c-1)A\frac{\partial^2\phi}{\partial x^2}$$

and the PDE associated with (24) reads

$$\frac{\partial U}{\partial t} + A\frac{\partial U}{\partial x} + h(c-1)\frac{A}{2}\frac{\partial^2 U}{\partial x^2} = 0 \tag{33}$$

As $c<1$, the diffusion coefficient $(c-1)A/2$ is negative and (24) is stable. We also deduce that the scheme will be diffusive. This undesired property is numerically illustrated in Section 6. It is then crucial to develop accurate schemes (step (iii) of Section 3.1). In the sequel, we show that the use of the QFESLM leads to less diffusive results.

DOI: 10.1002/fld

4.2. Quadrature methods

The method consisting in tracking the characteristic backward from an integration node has been studied by Oliveira and Baptista [11] using the Fourier analyis in the case of the linear transport equation with constant coefficients. A different approach is proposed here by employing the modified equation approach mentioned earlier.

4.2.1. Exact integration. For the one-dimensional advection problem (1), the RHS of (22) can be computed exactly when linear finite elements are used. Since $c<1$, we obtain

$$\begin{aligned}\int_\Omega U_h^n(x-\alpha_m(x))\phi_i\,\mathrm{d}x &= \sum_{j=1}^{d} U_j^n \int_0^1 \phi_j(x-\alpha_m(x))\phi_i\,\mathrm{d}x \\ &= U_{i-2}^n\int_0^1 \phi_{i-2}(x-\alpha_m(x))\phi_i\,\mathrm{d}x + U_{i-1}^n\int_0^1 \phi_{i-1}(x-\alpha_m(x))\phi_i\,\mathrm{d}x \\ &\quad + U_i^n\int_0^1 \phi_i(x-\alpha_m(x))\phi_i\,\mathrm{d}x + U_{i+1}^n\int_0^1 \phi_{i+1}(x-\alpha_m(x))\phi_i\,\mathrm{d}x \qquad (34)\end{aligned}$$

where d is the dimension of P_{1,Γ_0}. The integrals in the RHS of (34) are computed exactly (we have one-dimensional linear basis functions) and (34) leads to

$$\begin{aligned}\int_0^1 U^n(x-A\Delta t)\phi_i\,\mathrm{d}x &= \frac{hc^3}{6}U_{i-2}^n + \frac{h}{6}(1+3c+3c^2-3c^3)U_{i-1}^n \\ &\quad + \frac{h}{6}(4+3c^3-6c^2)U_i^n + \frac{h(1-c)^3}{6}U_{i+1}^n \qquad (35)\end{aligned}$$

Then by combining (22) and (35) we obtain

$$\begin{aligned}U_{i-1}^{n+1}+4U_i^{n+1}+U_{i+1}^{n+} &= U_{i-1}^n+4U_i^n+U_{i+1}^n+3c(U_{i-1}^n-U_{i+1}^n) \\ &\quad +3c^2(U_{i-1}^n-2U_i^n+U_{i+1}^n)+c^3(U_{i-2}^n-3U_{i-1}^n+3U_i^n-U_{i+1}^n) \qquad (36)\end{aligned}$$

By using the modified equation approach, we obtain the PDE associated with (36)

$$\frac{\partial U}{\partial t}+A\frac{\partial U}{\partial x}+h^3(c-1)^2\frac{cA}{24}\frac{\partial^4 U}{\partial x^4}=0 \qquad (37)$$

Owing to the term $h^3(c-1)^2(cA/24)\partial^4U/\partial x^4$, the scheme (36) is not dispersive and only weakly dissipative for large wave numbers. It thus seems reasonable to look for schemes based on precise integration of the RHS of (34). This is investigated in the sequel.

4.2.2. Numerical integration. The Gauss–Legendre and Gauss–Lobatto quadrature formulas are employed to compute the RHS of (34), and for a fixed integer i and integration point $\xi\in[-1,1]$,

DOI: 10.1002/fld

we let

$$\varpi^- = \frac{h\xi + x_{i-1} + x_i}{2}, \quad \varpi^+ = \frac{h\xi + x_i + x_{i+1}}{2} \tag{38}$$

We define $I_-^c = \{k \mid \xi_k \in [2c-3, 2c-1]\}$ and $I_+^c = \{k \mid \xi_k \in]2c-1, 2c+1]\}$, and we let nG and w_k be the number of integration points and weights, respectively. By using a Gaussian quadrature formula to evaluate the RHS of (22), we obtain

$$\begin{aligned}\frac{h}{6}(U_{i-1}^{n+1} + 4U_i^{n+1} + U_{i+1}^{n+1}) = {} & \frac{h}{4}\sum_{k=1}^{nG} w_k((1+\xi_k)U^n(\varpi_k^- - A\Delta t)) \\ & + \frac{h}{4}\sum_{k=1}^{nG} w_k((1-\xi_k)U^n(\varpi_k^+ - A\Delta t))\end{aligned} \tag{39}$$

As in the previous subsection, we consider one-dimensional linear basis functions in (34). We set

$$\begin{aligned}
B_{-2} &= \sum_{k\in I_-^c} w_k\left(c - \frac{1}{2} - \xi_k + \xi_k c - \frac{1}{2}\xi_k^2\right) \\
B_{-1} &= \sum_{k\in I_-^c} w_k(1 + 2\xi_k - 2\xi_k c + \xi_k^2) + \sum_{k\in I_+^c} w_k\left(c + \frac{1}{2} + \xi_k c - \frac{1}{2}\xi_k^2\right) \\
B_0 &= \sum_{k\in I_-^c} w_k\left(-c + \frac{3}{2} - \xi_k + \xi_k c - \frac{1}{2}\xi_k^2\right) + \sum_{k\in I_+^c} w_k(1 - 2\xi_k c + \xi_k^2) \\
B_{+1} &= \sum_{k\in I_+^c} w_k\left(-c + \frac{1}{2} + \xi_k c - \frac{1}{2}\xi_k^2\right)
\end{aligned} \tag{40}$$

After long and tedious algebra, we obtain

$$\begin{aligned}\tfrac{1}{6}(U_{i-1}^{n+1} + 4U_i^{n+1} + U_{i+1}^{n+1}) = {} & \tfrac{1}{2}(w_1 + w_{nG})(cU_{i-1}^n + (1-c)U_i^n) \\ & + \tfrac{1}{4}B_{-2}U_{i-2}^n + \tfrac{1}{4}B_{-1}U_{i-1}^n + \tfrac{1}{4}B_0U_i^n + \tfrac{1}{4}B_{+1}U_{i+1}^n\end{aligned} \tag{41}$$

The modified PDE is now used to perform a stability analysis of (41), which leads to

$$\frac{\partial U}{\partial t} + A\frac{\partial U}{\partial x} + h\frac{A}{c}\left(\frac{1}{6} + \frac{c^2}{2} - \frac{c}{4}(w_1 + w_{nG}) + \frac{1}{8}A_2\right)\frac{\partial^2 U}{\partial x^2} = 0 \tag{42}$$

where A_2 is defined as

$$A_2 = -\sum_{k\in I_+^c}(1 + 2c\xi_k - \xi_k^2)w_k + \sum_{k\in I_-^c}(1 - 4c - 2\xi_k c + \xi_k^2 + 2\xi_k)w_k$$

DOI: 10.1002/fld

The stability analysis of (41) depends on the coefficient of the last term in the LHS of (42)

$$\mathrm{SQ} \equiv \frac{A}{c}\left(\frac{1}{6}+\frac{c^2}{2}-\frac{c}{4}(w_1+w_{nG})\right)-\frac{A}{8c}\sum_{k\in I_+^c}(1+2c\xi_k-\xi_k^2)w_k$$

$$+\frac{A}{8c}\sum_{k\in I_-^c}(1-4c-2\xi_k c+\xi_k^2+2\xi_k)w_k \tag{43}$$

In (43), SQ depends on the employed Gauss–Legendre or Gauss–Lobatto quadrature formulas, which are exact for polynomials of order $2n+1$ and $2n-3$, respectively, when n integration points are considered. Therefore, we compare Gauss–Legendre and Gauss–Lobatto formulas with n and $n+1$ points, respectively, in the following.

SQ is now used to examine the influence of the numerical integration procedure on the stability properties of (41). The stability and instability regions are shown in Figure 2 and they correspond to $\mathrm{SQ}<0$ and $\mathrm{SQ}>0$, respectively, for the two Gaussian formulas and $n=2,3,4,9$. We observe that the area of the instability regions decreases as the number of quadrature points increase. The Gausss–Lobatto quadrature with n points leads to $n-2$ instability subregions while the Gausss–Legendre quadrature with n points leads to n instability subregions. This is in accordance with the result obtained in [11], where an amplification factor analysis is performed and is favourable to the use of the Gausss–Lobatto quadrature. This is to be expected since that quadrature is backward oriented.

The modified equation approach thus provides a theoretical framework to analyse the stability, accuracy and order of a given scheme, and this is an advantage over the amplification method, which is only restricted to numerical experiments as done in [11]. We now introduce the $\mathscr{C}^1$ interpolating schemes that are used at steps (iii) and (iv) of Sections 3.1 and 3.2, respectively.

5. THE $\mathscr{C}^1$-INTERPOLATING SCHEME

The accuracy of the first integral in the RHS of (13), and hence the advection term, strongly depends on the choice of an interpolation procedure for the semi-Lagrangian advection scheme [7, 17]. This has been mentioned previously at steps (iii) and (iv) for the ISLFEM and QSLFEM methods, respectively, in Section 3. McCalpin [24] and Purser and Leslie [13] have shown the importance of using high-order interpolating schemes. The bicubic spline interpolation has been found to be a good compromise between accuracy and computational cost for short-term simulations in the context of atmospheric models [13–15]. However, the method is restricted to regular meshes.

The kriging interpolating scheme has been used in [17] and yields equally favourable results on regular and unstructured meshes, showing its excellent flexibility. In [17] the computational cost of kriging was found significant and further elucidation of this question is needed. Further, to our knowledge, there is a lack of interpolation error analysis for the kriging scheme in the literature.

In order to try to construct an interpolating scheme on unstructured meshes at a reasonable computational cost, few $\mathscr{C}^1$-interpolating schemes are introduced as follows. These are the reduced Argyris finite element, namely the Bell finite element [19, 25], and the family of Clough and Tocher finite elements, complete and reduced [19, 26, 27].

DOI: 10.1002/fld

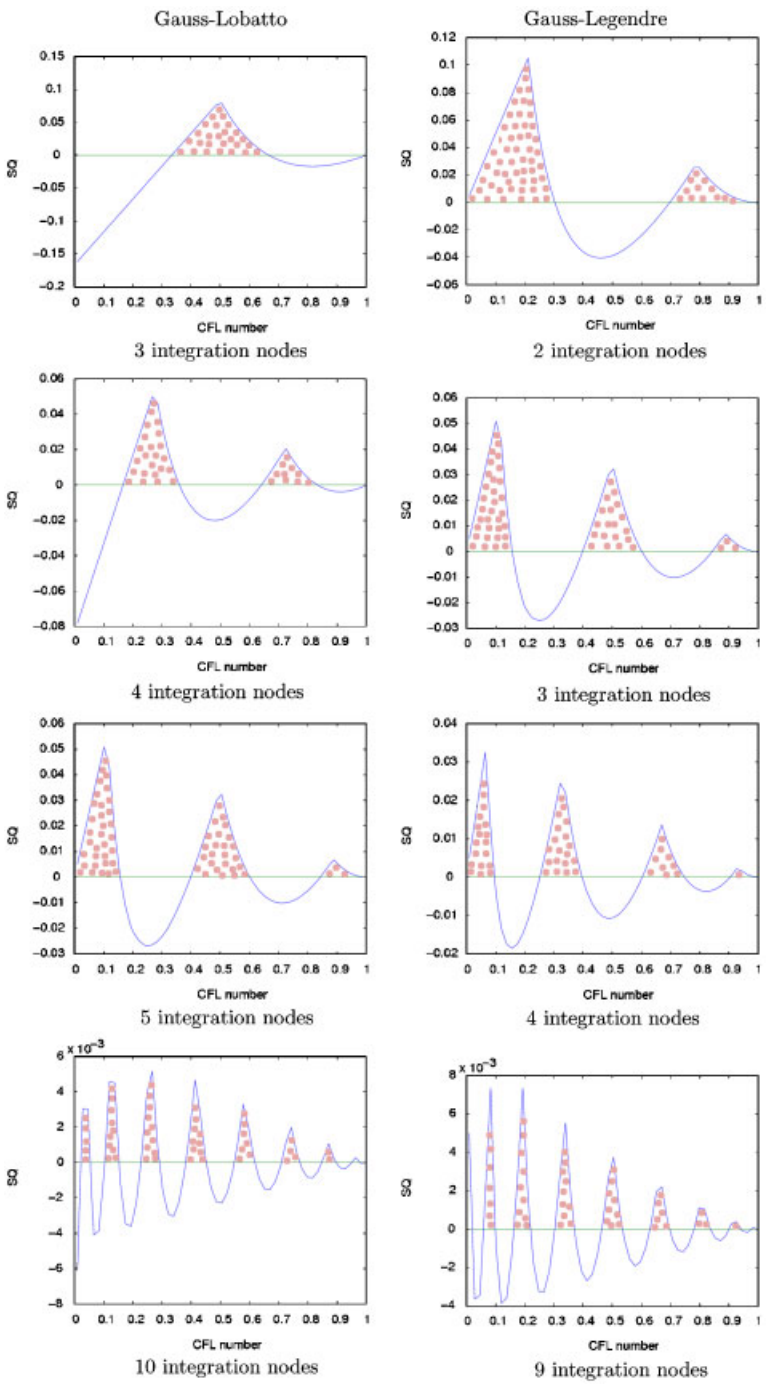

Figure 2. Diffusion coefficient as a function of the CLF number for Gauss–Legendre and Gauss–Lobatto quadratures.

DOI: 10.1002/fld

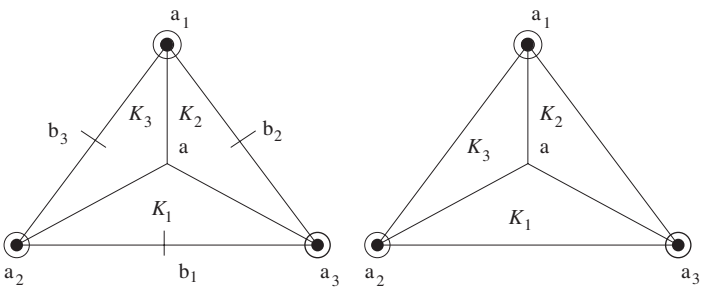

Figure 3. Set of degrees of freedom for the HCT-C (left) and HCT-R (right) finite elements.

5.1. The $\mathscr{C}^1$ quintic bell finite element

We let K a triangle of $\mathscr{L}_h$ and Σ_K be the set of degree of freedom on K. In the following, the variables ξ and η are associated with a reference element $\hat{K}$, while x and y refer to the current element and p is a function defined on the element K.

If $\mathbf{a}_i$, $1 \leqslant i \leqslant 3$, are the vertices of triangle $\hat{K}$, we have

$$\Sigma_{\hat{K}} = \left\{ p(\mathbf{a_i}), \frac{\partial p}{\partial \xi}(\mathbf{a_i}), \frac{\partial p}{\partial \eta}(\mathbf{a_i}), \frac{\partial^2 p}{\partial^2 \xi}(\mathbf{a_i}), \frac{\partial^2 p}{\partial \xi \partial \eta}(\mathbf{a_i}), \frac{\partial^2 p}{\partial^2 \eta}(\mathbf{a_i}), 1 \leqslant i \leqslant 3 \right\}$$

and the local interpolation operator $\Pi_{\hat{K}}^{\text{Bell}}$ is defined for all $p \in \mathscr{C}^1(\bar{\hat{K}})$ by

$$\Pi_{\hat{K}}^{\text{Bell}} p = \sum_{i=1}^{18} p(\mathbf{a}_i)\phi_i$$

where the basis functions ϕ_i of the Bell finite element are detailed in [25]. At each vertex $\mathbf{a}_i$, the nodal value $p(\mathbf{a_i})$, the first and second derivatives are known.

5.2. The $\mathscr{C}^1$ cubic HCT element

The HCT elements are also called composite finite elements and they are defined as follows. Triangle K with vertices $\mathbf{a}_i$, $i = 1, 2, 3$, is subdivided into three subtriangles K_i, $i = 1, 2, 3$, as shown in Figure 3 where $\mathbf{a}$ is an arbitrary point. Let $\mathbf{v}_i$ be the unit exterior normal of the edge opposite to $\mathbf{a}_i$. We denote by $\mathbf{b}_i$, $i = 1, 2, 3$, the mid-side node of the face that does not contain $\mathbf{a}_i$, and $\mathbf{c}_i$, $i = 1, 2, 3$, the orthogonal projection of $\mathbf{a}_i$ on the face containing $\mathbf{b}_i$, $i = 1, 2, 3$. Further, in the following the indices are in the set $\{1, 2, 3\}$ (modulo 3).

The derivative of p in the direction $\mathbf{a_i a_{i+2}}$ is defined as

$$Dp(\mathbf{a_i}) \cdot \mathbf{a_i a_{i+2}} = (x_{i+2} - x_i)\frac{\partial p}{\partial x}(\mathbf{a_i}) + (y_{i+2} - y_i)\frac{\partial p}{\partial y}(\mathbf{a_i}) \tag{44}$$

where (x_i, y_i) are the Cartesian coordinates of $\mathbf{a_i}$, $i = 1, 2, 3$. The set of degrees of freedom for the complete HCT element (HCT-C) (shown in Figure 3) is

$$\Sigma_K = \{p(\mathbf{a_i}), Dp(\mathbf{a_i}) \cdot \mathbf{a_i a_{i+2}}, Dp(\mathbf{a_i}) \cdot \mathbf{a_i a_{i+1}}, Dp(\mathbf{b_i}) \cdot \mathbf{c_i a_i}, 1 \leqslant i \leqslant 3\}$$

DOI: 10.1002/fld

For all p in $\mathscr{C}^1(\bar{K})$ and $i=1,2,3$, the local interpolation operator $\Pi_K^{\text{HCT-C}}$ is defined as

$$\Pi_{K_i}^{\text{HCT-C}} p = \sum_{j=i}^{i+2} p(\mathbf{a_j})\phi_{i,j}^0 + Dp(\mathbf{a_j})\cdot\mathbf{a_j}\mathbf{a_{j+2}}\phi_{i,j,j+2}^1 + Dp(\mathbf{a_j})\cdot\mathbf{a_j}\mathbf{a_{j+1}}\phi_{i,j,j+1}^1 + Dp(\mathbf{b_j})\cdot\mathbf{c_j}\mathbf{a_j}\phi_{i,j}^{\perp}$$

At each vertex $\mathbf{a_i}$, the degrees of freedom are nodal values $p(\mathbf{a_i})$ and the directional derivatives $Dp(\mathbf{a_i})\cdot\mathbf{a_i}\mathbf{a_j}$. The basis functions of the HCT-C element, $\phi^0, \phi^1, \phi^{\perp}$ are given in the Appendix. Their implementation is detailed in [27].

We will also use the reduced HCT element (HCT-R) (shown in Figure 3), which is derived from the complete one by removing normal derivatives. The set of the degrees of freedom for the HCT-R element is thus

$$\Sigma_K = \{p(\mathbf{a_i}),\, Dp(\mathbf{a_i})\cdot\mathbf{a_i}\mathbf{a_{i+2}},\, Dp(\mathbf{a_i})\cdot\mathbf{a_i}\mathbf{a_{i+1}},\, 1\leqslant i\leqslant 3\}$$

and the local interpolation operator $\Pi_K^{\text{HCT-R}}$ is defined as

$$\Pi_{K_i}^{\text{HCT-R}} p = \sum_{j=i}^{i+2} p(\mathbf{a_i})\tilde{\phi}_{i,j}^0 + Dp(\mathbf{a_i})\cdot\mathbf{a_j}\mathbf{a_{j+2}}\tilde{\phi}_{i,j,j+2}^1 + Dp(\mathbf{a_i})\cdot\mathbf{a_j}\mathbf{a_{j+1}}\tilde{\phi}_{i,j,j+1}^1 \tag{45}$$

The basis functions of the HCT-R element, $\tilde{\phi}^0, \tilde{\phi}^1$ are given in the Appendix and their implementation is detailed in [27]. Interpolation error estimates and $\mathscr{C}^1$ continuity are obtained in [19] for the HCT-C and HCT-R elements.

5.3. *Explicit construction of $\mathscr{C}^1$-interpolating scheme*

Finite elements of class $\mathscr{C}^1$ require the computation of the derivatives. In order to avoid such computation, we let $\mathscr{H}_h$ be a $\mathscr{C}^1$ finite-element space and we denote by π the L^2-projector on $\mathscr{H}_h$ defined in the following way. Given U^n in L^2, $\pi(U^n)$ is the solution of the variational problem

$$\int_\Omega \pi(U^n)\phi_h \,\mathrm{d}\mathbf{x} \equiv \int_\Omega U^n\phi_h \,\mathrm{d}\mathbf{x} \quad \forall\phi_h \in \mathscr{H}_h \tag{46}$$

In the sequel, the space $\mathscr{H}_h$ is either the finite-element space associated with the Bell or HCT (reduced or complete) elements. To describe a given $\mathscr{C}^1$-interpolating scheme, we first solve (46) in order to determine the values of the degrees of freedom and then use the local interpolation operator. The interpolation procedure is cost effective. Comparison of the computational cost for the above interpolating schemes is done in the next section.

6. NUMERICAL RESULTS

In this section we perform advection experiments and solve (11) with $f=0$. The velocity field $\mathbf{A}$ is assumed constant in time and it is associated with a solid body rotation such that

$$\mathbf{A} = \omega(-y, x) \tag{47}$$

DOI: 10.1002/fld

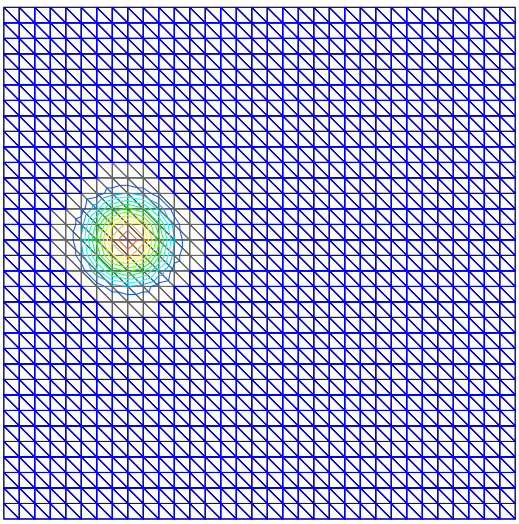

Figure 4. The regular 34×34 mesh and the initial cosine hill.

with a angular frequency $\omega = 10^{-5}\,\mathrm{s}^{-1}$. All experiments are performed on a regular 34×34 grid centred at the point $(19, 9)$ with $h = 10\,\mathrm{km}$, and the initial cosine hill

$$U_0(x, y) = \begin{cases} 50\left(1 + \cos\left(\dfrac{\pi R}{4h}\right)\right), & R \leqslant 4h \\ 0 & \text{otherwise} \end{cases} \tag{48}$$

where $R^2 = x^2 + y^2$ is shown in Figure 4. The CFL number ($c = \max|V|\Delta t / h$) is set to one, where $\max|V|$ is the maximum speed at the four corners of the domain. The values of h and ω are chosen so that a comparison can be made with the results obtained in [17]. One rotation of the cosine hill corresponds to 142 times steps. The semi-Lagrangian scheme (12) is then rewritten as

$$U(\mathbf{x}_m, t_n + \Delta t) = U(\mathbf{x}_m - \boldsymbol{\alpha}_m, t_n) \tag{49}$$

The exact displacements $\boldsymbol{\alpha}_m$ are calculated from (4) and (47)

$$\boldsymbol{\alpha}_m = \begin{pmatrix} x_m(1 - \cos(\omega\Delta t)) - y_m \sin(\omega\Delta t) \\ y_m(1 - \cos(\omega\Delta t)) + x_m \sin(\omega\Delta t) \end{pmatrix} \tag{50}$$

where $\mathbf{x}_m = (x_m, y_m)$ is the position vector at the arrival point. In the following exact displacements are used in order to focus on the loss of accuracy in evaluating upstream tracer values (steps (iii) and (iv) of Sections 3.1 and 3.2, respectively) and not on the loss of accuracy of the computed displacements. The evaluation of upstream tracer values is done via the linear, quadratic and the Bell, HCT-C and HCT-R $\mathscr{C}^1$-interpolation schemes. The finite-element scheme (with basis functions ϕ_h in P_{k,Γ_0}) that is employed in (13) and used at steps (iv) and (iii) of Sections 3.1 and 3.2 for the ISLFEM and QSLFEM, respectively, is named here P_1- and P_2-*Formulation* for $k = 1, 2$, respectively. At initial time, the maximum and minimum values of the

DOI: 10.1002/fld

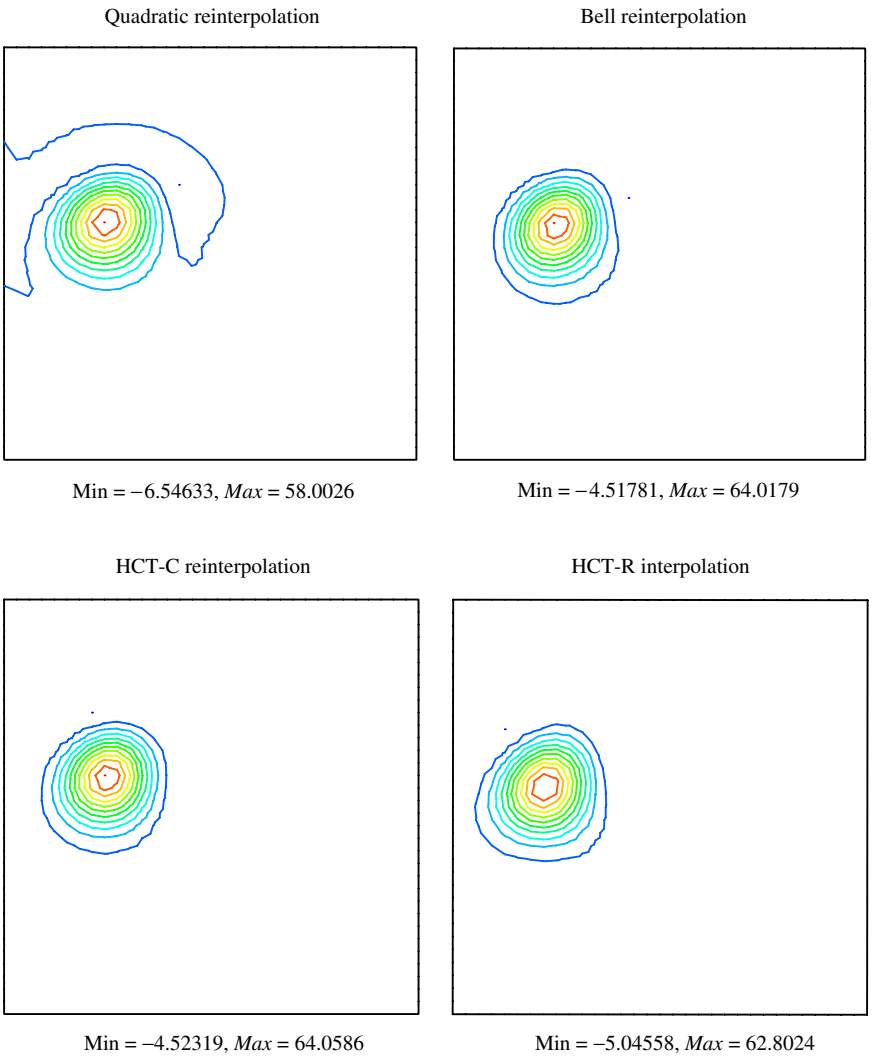

Figure 5. Shape of the cosine hill after 5 rotations using the ISLFEM method and the P_2-Formulation.

cosine hill are Max = 100 and Min = 0, respectively. These values should be preserved during the simulation.

For the ISLFEM method and the P_1-Formulation, the cosine hill has lost more than 88% of its amplitude for all interpolating schemes, after only one rotation. This is why the results are not displayed here. For the P_2-Formulation, the cosine hill is shown in Figure 5 after 5 rotations for the quadratic, Bell, HCT-C and HCT-R interpolation schemes. The cosine hill loses more than 35% of its amplitude for all schemes and the dispersion ranges from 4.5 to 6.5%. These results are comparable to those obtained in [17] using bicubic spline interpolation. If the simulation is

DOI: 10.1002/fld

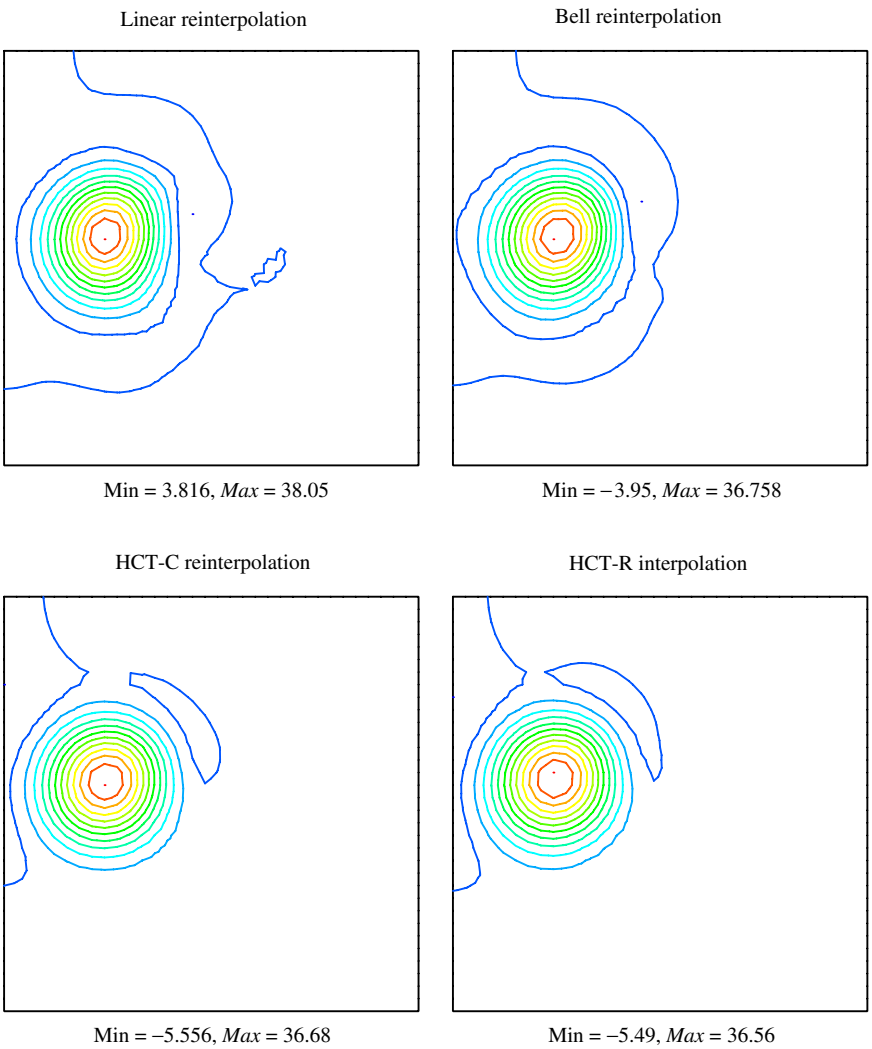

Figure 6. Similar to Figure 5 but for the QSLFEM method and the P_1-Formulation after 25 rotations.

performed for more than 5 rotations, numerical dispersion causes the cosine hill to reach the boundary, generating boundary problems due to the open boundary. The experiment then loses its validity.

For the QSLFEM and the P_1-Formulation, the cosine hill is shown in Figure 6 after 25 rotations. The hill has lost more than 60% of its amplitude for all schemes (linear, Bell, HCT-C and HCT-R) and the numerical dispersion ranges from 4 to 5.5%. The significant level of damping is mainly due to the use of the P_1-Formulation. However, these results have much less damping than those obtained using the ISLFEM. In Figure 7 the hill is shown after 50 rotations for the P_2-Formulation. The level of damping is only 4% for the finite element using quadratic approximation, 8% for

DOI: 10.1002/fld

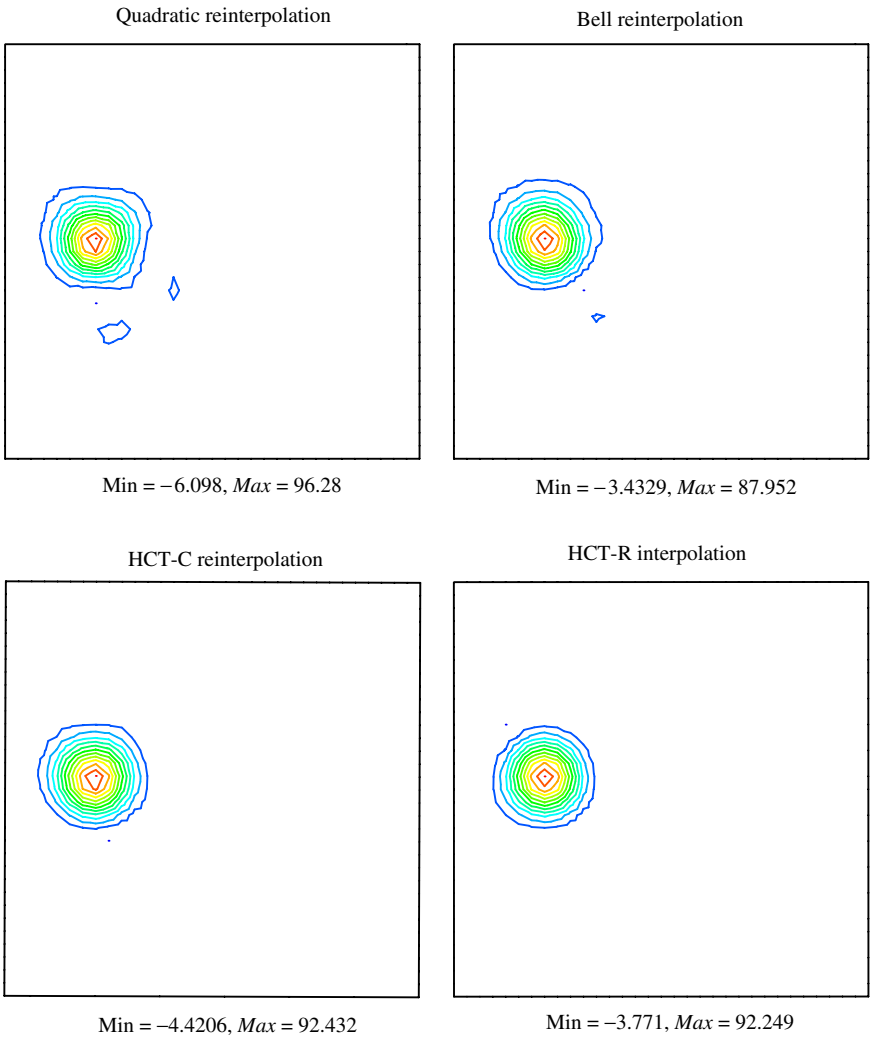

Figure 7. Similar to Figure 6 but for P_2-Formulation after 50 rotations.

the HCT schemes and 12% for the Bell one, and the dispersion is between 3.5 and 6% for all schemes. The solutions are displayed in Figures 8 and 9 up to 25 and 50 rotations for the P_1- and P_2-Formulations, respectively. These results compared well with those obtained in [17] when employing the kriging interpolation scheme. Note that although the quadratic approximation for both the interpolation scheme and the P_2-Formulation gives less damping than the $\mathscr{C}^1$ interpolators in Figure 7, we can observe that it is somewhat more dispersive. This effect is greatly amplified for nonlinear advection as it is demonstrated in [28], where the application of $\mathscr{C}^1$ interpolation schemes are investigated for nonlinear semi-Lagrangian shallow-water models.

DOI: 10.1002/fld

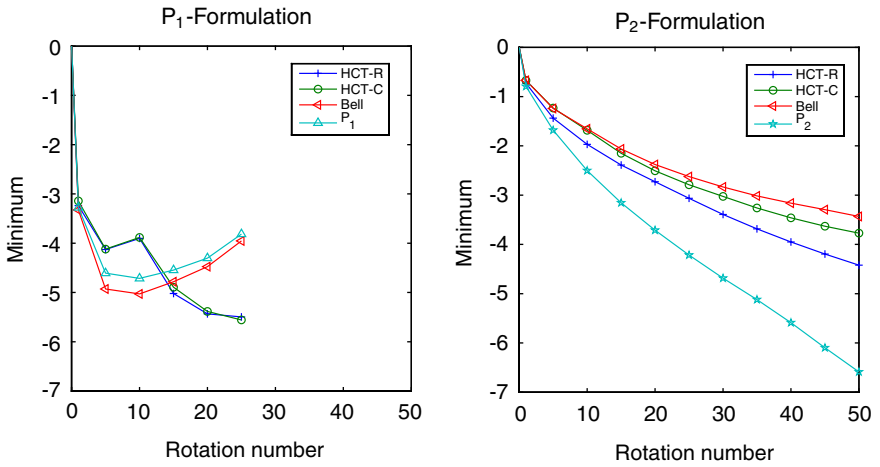

Figure 8. Minimum values of the cosine hill for the QSLFEM method and the P_1- and P_2-Formulations.

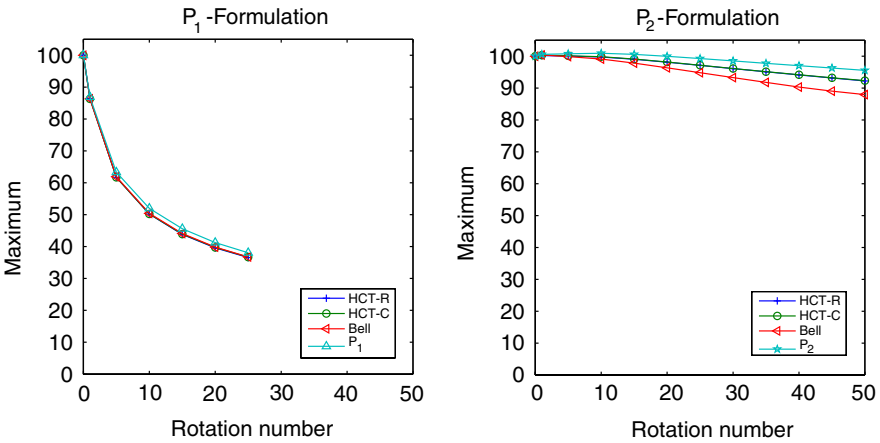

Figure 9. Similar to Figure 8 but for the maximum of the cosine hill.

The root mean square (RMS) error between the numerical and initial cosine hills is defined as

$$\mathrm{RMS} = \left(\int_\Omega (U - U_0)^2 \, \mathrm{d}\mathbf{x}\right)^{1/2} \Bigg/ \left(\int_\Omega U_0^2 \, \mathrm{d}\mathbf{x}\right)^{1/2}$$

and it is shown in Figure 10 for the QSLFEM and the P_1- and P_2-Formulations. For the P_1-Formulation, the RMS is more than 60% for all schemes (linear, Bell, HCT-C and HCT-R) after 25 rotations. For the P_2-Formulation we obtain RMS = 35% for the HCT-R scheme and the RMS ranges from 13 to 15% for the quadratic, HCT-C and Bell schemes, respectively, after 50 rotations. The results for the ISLFEM are not presented here since after only 5 rotations the RMS

DOI: 10.1002/fld

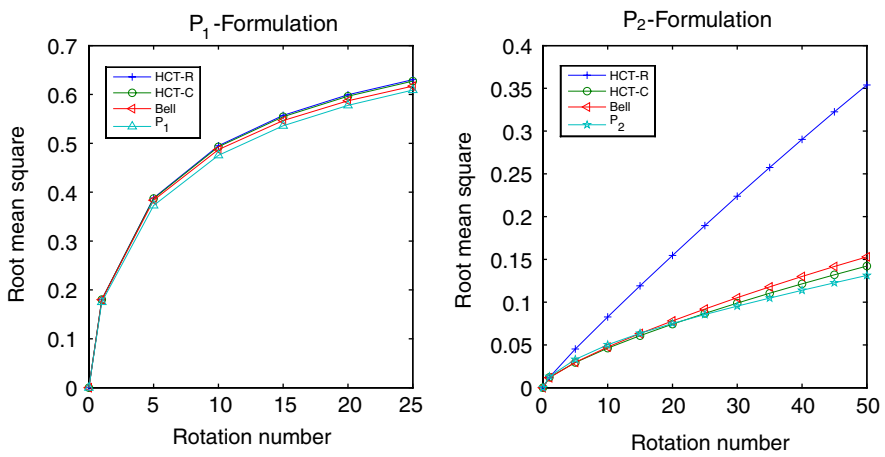

Figure 10. Similar to Figure 8 but for the RMS error between the numerical and initial solutions.

is more than 40% for all schemes. The experiment loses its validity after 10 rotations due to the interaction between the cosine hill and the open boundary.

In semi-Lagrangian schemes, mass conservation is an important issue [29, 30]. To address this problem in the context of $\mathscr{C}^1$-interpolating schemes, we define the mass variation (MV) as

$$\mathrm{MV} = \int_\Omega U \,\mathrm{d}\mathbf{x} \Big/ \int_\Omega U_0 \,\mathrm{d}\mathbf{x}$$

and MV is shown in Figure 11 for the linear, quadratic, Bell, HCT-C and HCT-R interpolating schemes. After 25 rotations and using the P_1-Formulation the loss of mass is about 5% for all schemes. When the P_2-Formulation is employed, the HCT-R and Bell formulations have a loss of, respectively, 3.5 and 6.5% after 50 rotations, while the quadratic finite element and the HCT-C schemes exhibit a gain in mass of about 0.05 and 4%, respectively.

The computational cost is also an important issue. For the $\mathscr{C}^1$ interpolators presented in this paper, the matrix appearing in the LHS of (46) is computed once so that the LU decomposition is done only once and its cost becomes negligibly small once it is spread over a large number of time steps. For a single field and a mesh of N nodes, there are hence $O(N)$ operations in the calculation of $\pi(U^n)$ in (46) per node. The $\mathscr{C}^1$ interpolators are clearly more expensive than bicubic spline interpolation. Indeed, Bermejo [22] found that the computation of the upstream value of a scalar field using bicubic spline interpolation requires 49 operations if it is implemented efficiently. However, as shown in [28], the $\mathscr{C}^1$ interpolators also give good results on unstructured meshes for nonlinear semi-Lagrangian advection while the bicubic spline interpolator is restricted to regular meshes.

Finally, the above numerical tests have also been performed using numerically computed displacements, and results similar to those presented here have been obtained.

DOI: 10.1002/fld

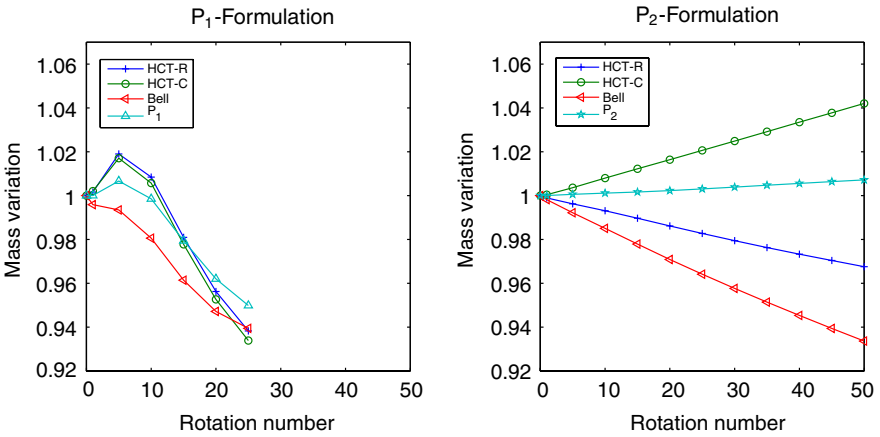

Figure 11. Similar to Figure 8 but for the mass variation MV.

7. CONCLUDING REMARKS

This paper addresses the combination of $\mathscr{C}^1$-interpolating schemes and characteristic backward tracking from quadratures nodes, for semi-Lagrangian advection problems. A stability analysis is performed based on the modified equation approach in the case of the one-dimensional linear advection. It reveals that the QSLFEM induces less dissipation than the ISLFEM, but the former may lead to unstable solutions. Those could, however, be avoided by increasing the number of integration nodes. In the test problem, a cosine hill is advected in a rotational flow field. The results obtained with the QSLFEM are found close to the kriging ones and are much more accurate than those computed using bicubic spline interpolation. The computational cost of the method is in $O(N)$ operations per node for a single field and a mesh of N nodes, and hence much more expansive than bicubic spline interpolation. However, the latter is restricted to regular meshes while the $\mathscr{C}^1$ interpolators presented here also give good results on unstructured meshes for nonlinear semi-Lagrangian advection as shown in [28].

APPENDIX

We let $r_j = A_j \lambda,\ j = 1, 2$, where the matrices r_1 and r_2 are the basis functions of subtriangle K_i for the HCT-C and HCT-R elements, respectively, with

$$r_1 = (r^0_{i,i}, r^0_{i,i+1}, r^0_{i,i+2}, r^1_{i,i,i+2}, r^1_{i,i,i+1}, r^1_{i,i+1,i}, r^1_{i,i+1,i+2}, r^1_{i,i+2,i+1}, r^1_{i,i+2,i}, r^\perp_{i,i}, r^\perp_{i,i+1}, r^\perp_{i,i+2})$$

$$r_2 = r^0_{i,i}, r^0_{i,i+1}, r^0_{i,i+2}, r^1_{i,i,i+2}, r^1_{i,i,i+1}, r^1_{i,i+1,i}, r^1_{i,i+1,i+2}, r^1_{i,i+2,i+1}, r^1_{i,i+2,i})$$

$$\lambda = (\lambda^3_i, \lambda^3_{i+1}, \lambda^3_{i+2}, \lambda^2_i \lambda_{i+2}, \lambda 2_i \lambda_{i+1}, \lambda^2_{i+1} \lambda_i, \lambda^2_{i+1} \lambda_{i+2}, \lambda^2_{i+2} \lambda_{i+1}, \lambda^2_{i+2} \lambda_i, \lambda_i \lambda_{i+1} \lambda_{i+2})$$

DOI: 10.1002/fld

$$A_1=\begin{bmatrix}
-\frac{1}{2}(e_{i+1}-e_{i+2}) & 0 & 0 & \frac{3}{2}(3+e_{i+1}) & \frac{3}{2}(3-e_{i+2}) & 0 & 0 & 0 & 0 & 0\\
\frac{1}{2}(1-2e_i-e_{i+2}) & 1 & 0 & -\frac{3}{2}(1-e_i) & \frac{3}{2}(e_i+e_{i+2}) & 3 & 3 & 0 & 0 & 3(1-e_i)\\
\frac{1}{2}(1+2e_i+e_{i+1}) & 0 & 1 & -\frac{3}{2}(e_i+e_{i+1}) & -\frac{3}{2}(1+e_i) & 0 & 0 & 3 & 3 & 3(1+e_i)\\
-\frac{1}{12}(1+e_{i+1}) & 0 & 0 & \frac{1}{4}(7+e_{i+1}) & -\frac{1}{2} & 0 & 0 & 0 & 0 & 0\\
-\frac{1}{12}(1-e_{i+2}) & 0 & 0 & -\frac{1}{2} & \frac{1}{4}(7-e_{i+2}) & 0 & 0 & 0 & 0 & 0\\
\frac{1}{12}(7+e_{i+2}) & 0 & 0 & \frac{1}{2} & -\frac{1}{4}(5+e_{i+2}) & 1 & 0 & 0 & 0 & -1\\
\frac{1}{6}(4-e_i) & 0 & 0 & -\frac{1}{4}(3-e_i) & -\frac{1}{4}(5-e_i) & 0 & 1 & 0 & 0 & \frac{1}{2}(3-e_i)\\
\frac{1}{6}(4+e_i) & 0 & 0 & -\frac{1}{4}(5+e_i) & -\frac{1}{4}(3+e_i) & 0 & 0 & 1 & 0 & \frac{1}{2}(3+e_i)\\
-\frac{1}{12}(7-e_{i+1}) & 0 & 0 & \frac{1}{4}(5-e_{i+1}) & \frac{1}{2} & 0 & 0 & 0 & 1 & -1\\
\frac{4}{3} & 0 & 0 & -2 & -2 & 0 & 0 & 0 & 0 & 4\\
-\frac{2}{3} & 0 & 0 & 2 & 0 & 0 & 0 & 0 & 0 & 0\\
-\frac{2}{3} & 0 & 0 & 0 & 2 & 0 & 0 & 0 & 0 & 0
\end{bmatrix}$$

$$A_2=\begin{bmatrix}
-\frac{1}{2}(e_{i+1}-e_{i+2}) & 0 & 0 & \frac{3}{2}(3+e_{i+1}) & \frac{3}{2}(3-e_{i+1}) & 0 & 0 & 0 & 0 & 0\\
\frac{1}{2}(1-2e_i-e_{i+2}) & 1 & 0 & -\frac{3}{2}(1-e_i) & -\frac{3}{2}(e_i+e_{i+2}) & 3 & 3 & 0 & 0 & 3(1-e_i)\\
\frac{1}{2}(1+2e_i+e_{i+1}) & 0 & 1 & -\frac{3}{2}(e_i+e_{i+2}) & -\frac{3}{2}(1+e_i) & 0 & 0 & 3 & 3 & 3(1+e_i)\\
-\frac{1}{4}(1+e_{i+1}) & 0 & 0 & \frac{1}{4}(5+3e_{i+1}) & \frac{1}{2} & 0 & 0 & 0 & 0 & 0\\
-\frac{1}{4}(1-e_{i+2}) & 0 & 0 & \frac{1}{2} & \frac{1}{4}(5-3e_{i+2}) & 0 & 0 & 0 & 0 & 0\\
\frac{1}{4}(1-e_{i+2}) & 0 & 0 & -\frac{1}{2} & -\frac{1}{4}(1-e_{i+2}) & 1 & 0 & 0 & 0 & 1\\
\frac{1}{2}e_i & 0 & 0 & -\frac{1}{4}(1-3e_i) & \frac{1}{4}(1+e_i) & 0 & 1 & 0 & 0 & \frac{1}{2}(1-3e_i)\\
\frac{1}{2}e_i & 0 & 0 & \frac{1}{4}(1-e_i) & -\frac{1}{4}(1+e_i) & 0 & 0 & 1 & 0 & \frac{1}{2}(1+3e_i)\\
\frac{1}{4}(1+e_{i+1}) & 0 & 0 & -\frac{1}{4}(1-3e_{i+1}) & \frac{1}{2} & 0 & 0 & 0 & 1 & 1
\end{bmatrix}$$

The parameters λ_i (resp. e_i), $i=1,2,3$, are the barycentric coordinates (resp. the excentricity parameters) of triangle K. The excentricity parameters e_i are defined as

$$e_i=\frac{l_{i+2}^2-l_{i+1}^2}{l_i^2} \quad \text{with } l_i=\sqrt{(x_{i+2}-x_{i+1})^2+(y_{i+2}-y_{i+1})^2},\ \ i=1,2,3 \tag{A1}$$

ACKNOWLEDGEMENTS

This work was supported by grants from the Natural Sciences and Engineering Research Council (NSERC) and grants from the Fonds québécois de la recherche sur la nature et les technologies (FQRNT). The use of the computing facilities of the Groupe Interdisciplinaire de Recherche en Éléments Finis (GIREF) is also acknowledged.

DOI: 10.1002/fld

REFERENCES

1. Baptista AM. Solution of advection-dominated transport by Eulerian–Lagrangian methods using the backwards method of characteristics. *Ph.D. Dissertation*, Massachusetts Institute of Technology, Cambridge, MA, 1987.
2. Morton KW, Priesttyl A, Suli E. Stability of the Lagrange–Galerkin method with non-exact integration. *Mathematical Modelling and Numerical Analysis* 1988; **22**:625–653.
3. Pironneau O. *Méthodes des éléments finis pour les fluides*. Masson: Paris, 1988.
4. Pironneau O, Liou J, Tezduyar T. Characteristic-Galerkin and Galerkin/least-squares space–time formulation for the advection–diffusion equation with time-dependent domains. *Computer Methods in Applied Mechanics and Engineering* 1992; **100**:117–141.
5. Robert A. A stable numerical integration scheme for the primitive meteorological equations. *Atmosphere–Ocean* 1981; **19**:35–46.
6. Robert A. A semi-Lagrangian and semi-implicit numerical integration scheme for the primitive meteorological equations. *Japan Meteorological Society* 1982; **60**:319–325.
7. Staniforth A, Côté J. Semi-Lagrangian integration schemes for atmospheric models: a review. *Monthly Weather Review* 1991; **119**:2206–2223.
8. Benque JP, Labadie G, Ronat T. A new finite element method for Navier–Stokes equations coupled with a temperature equation. In *Finite Element Methods in Flow Problems; Proceedings of the 4th International Symposium on Finite Elements in Flow Problems,* Tokyo, Japan, 26–29 July 1982, Kawai T (ed.). University of Tokyo Press/North-Holland Publishing Co.: Tokyo/Amsterdam, 1982; 295–301.
9. Douglas J, Russel TF. Numerical methods for convection-dominated diffusion problems based on combining the methods of characteristics with finite element methods or finite difference procedures. *SIAM Journal on Numerical Analysis* 1982; **19**:871–885.
10. Morton KW. Generalized Galerkin methods for hyperbolic problems. *Computer Methods in Applied Mechanics and Engineering* 1985; **52**:847–871.
11. Oliveira A, Baptista AM. A comparison of the integration and interpolation Eulerian–Lagrangian methods. *International Journal for Numerical Methods in Fluids* 1995; **21**:183–204.
12. Staniforth A, Temperton C. Semi-implicit semi-Lagrangian integration schemes for a barotropic finite-element regional model. *Monthly Weather Review* 1986; **114**:2078–2090.
13. Purser RJ, Leslie LM. A semi-implicit semi-Lagrangian finite difference scheme using high order spatial differencing on a nonstaggered grid. *Monthly Weather Review* 1988; **116**:2069–2080.
14. Bates JR, McDonald A. Multiply-upstream, semi-Lagrangian advective schemes: analysis and application to a multilevel primitive equation. *Monthly Weather Review* 1982; **11**:1831–1842.
15. Pudykiewicz J, Staniforth A. Some properties and comparative performances of the semi-Lagrangian method in the solution of the advection-diffusion equation. *Atmosphere–Ocean* 1984; **22**:283–308.
16. Purnell DK. Solution of the advective equation by upstream interpolation with cubic spline. *Monthly Weather Review* 1976; **104**:42–48.
17. Le Roux DY, Lin CA, Staniforth A. An accurate interpolating scheme for semi-Lagrangian advection on an unstructured mesh for ocean modelling. *Tellus* 1997; **49**:119–138.
18. Le Roux DY, Lin C, Staniforth A. A semi-implicit semi-Lagrangian finite-element shallow-water ocean model. *Monthly Weather Review* 2000; **128**:1384–1401.
19. Ciarlet PG, Lions JL. *Handbook of Numerical Analysis*, *Finite Element Methods* (*Part 1*), vol. 2. North-Holland: Amsterdam, 1991.
20. Warming RF, Hyett BJ. The modified equation approach to the stability and accuracy analysis of finite-difference methods. *Journal of Computational Physics* 1974; **14**:159–179.
21. Temperton C, Staniforth A. An efficient two-time level semi-Lagrangian semi-implicit integration scheme. *Quarterly Journal of the Royal Meteorological Society* 1987; **113**:1025–1039.
22. Bermejo R. On the equivalence of semi-Lagrangian and particle-in-cell finite element methods. *Monthly Weather Review* 1990; **118**:979–987.
23. Pudykiewicz J, Benoit R, Staniforth A. Preliminary results from a partial LRTAP model based on an existing meteorological forecast model. *Atmosphere–Ocean* 1985; **23**:267–303.
24. McCalpin JD. A quantitative analysis of the dissipation inherent in semi-Lagrangian advection. *Monthly Weather Review* 1984; **112**:1267–1275.
25. Dhatt G, Touzot G. Une présentation de la méthode des éléments finis. *Les presses de l'Université Laval*, Sainte-Foy, 1981.

DOI: 10.1002/fld

26. Bernadou M, Boisserie JM, Kamal H. Sur l'implementation des éléments finis de Hseih–Clough–Tocher complèt et réduit. *INRIA. Rapport de recherche*, vol. 4, 1980.
27. Bernadou M, Kamal H. Basis functions for the general Hseih–Cloug–Tocher triangles, complete or reduced. *INRIA. Rapport de recherche*, vol. 5, 1980.
28. Djoumna G, Le Roux DY, Pierre R. High-order $\mathscr{C}^1$ finite-element interpolating schemes. Part II: For nonlinear semi-Lagrangian shallow-water models. *International Journal for Numerical Methods in Fluids* 2007; DOI: 10.1002/fld.1687.
29. Bermejo R, Conde J. A conservative quasi-monotone semi-Lagrangian scheme. *Monthly Weather Review* 2002; **130**:423–430.
30. Gravel S, Staniforth A. A mass conserving semi-Lagrangian scheme for the shallow water equations. *Monthly Weather Review* 1994; **122**:243–248.